ACS NANO

www.acsnano.org

ARTICLE

Understanding and Mapping Sensitivity in MoS_2 Field-Effect-Transistor-Based Sensors

Steven G. Noyce, James L. Doherty, Stefan Zauscher, and Aaron D. Franklin*

Cite This: *ACS Nano* 2020, 14, 11637−11647

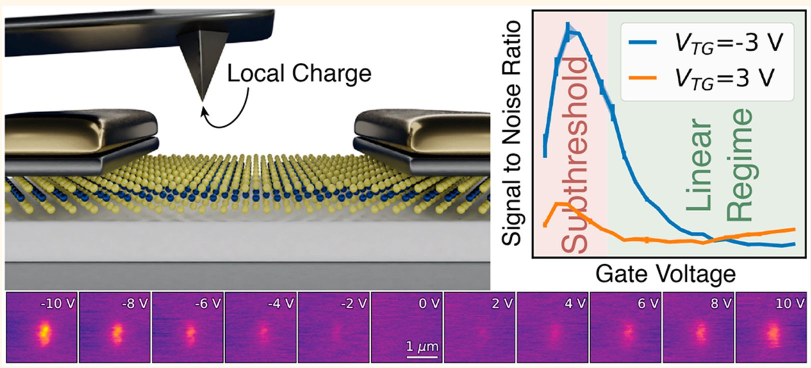

ABSTRACT: **Sensors based on two-dimensional (2D) field-effect transistors (FETs) are extremely sensitive and can detect charged analytes with attomolar limits of detection (LOD). Despite some impressive LODs, the operating mechanisms and factors that determine the signal-to-noise ratio in 2D FET-based sensors remain poorly understood. These uncertainties, coupled with an expansive design space for sensor layout and analyte positioning, result in a field with many reported highlights but limited collective progress. Here, we provide insight into sensing mechanisms of 2D molybdenum disulfide (MoS_2) FETs by realizing precise control over the position and charge of an analyte using a customized atomic force microscope (AFM), with the AFM tip acting as an analyte. The sensitivity of the MoS_2 FET channel is revealed to be nonuniform, manifesting sensitive hotspots with locations that are stable over time. When the charge of the analyte is varied, an asymmetry is observed in the device drain−current response, with analytes acting to turn the device off leading to a 2.5× increase in the signal-to-noise ratio (SNR). We developed a numerical model, applicable to all FET-based charge-detection sensors, that confirms our experimental observation and suggests an underlying mechanism. Further, extensive characterization of a set of different MoS_2 FETs under various analyte conditions, coupled with the numerical model, led to the identification of three distinct SNRs that peak with dependence on the layout and operating conditions used for a sensor. These findings reveal the important role of analyte position and coverage in determining the optimal operating bias conditions for maximal sensitivity in 2D FET-based sensors, which provides key insights for future sensor design and control.**

KEYWORDS: *sensor, field-effect transistor, molybdenum disulfide, 2D, signal-to-noise ratio, hotspot, sensing mechanism*

Sensors based on 2D materials offer extreme sensitivities, largely due to their high surface-to-volume ratios enabling efficient gating by nearby, analyte-based charges.[1] Graphene was the first 2D material to gain prominence as a sensing element and was eventually shown to be capable of resolving the adsorption of a single gas molecule,[2] among other achievements.[3−6] Limitations arising from the lack of a bandgap in graphene led to increased work in sensors based on semiconducting 2D materials, such as phosphorene,[7] tellurene,[8] or molybdenum disulfide (MoS_2).[9,10] The achievements of these semiconducting nanomaterial-based sensors are notable, including attomolar limits of detection and label-free sensing.[11] These achievements have been obtained while avoiding the pitfalls of competing technologies; for example, the high operation temperature and power consumption required by metal-oxide-semiconductor (MOS) gas sensors.[12] 2D material-based

Received: May 19, 2020
Accepted: August 12, 2020
Published: August 12, 2020

https://dx.doi.org/10.1021/acsnano.0c04192
ACS Nano 2020, 14, 11637−11647

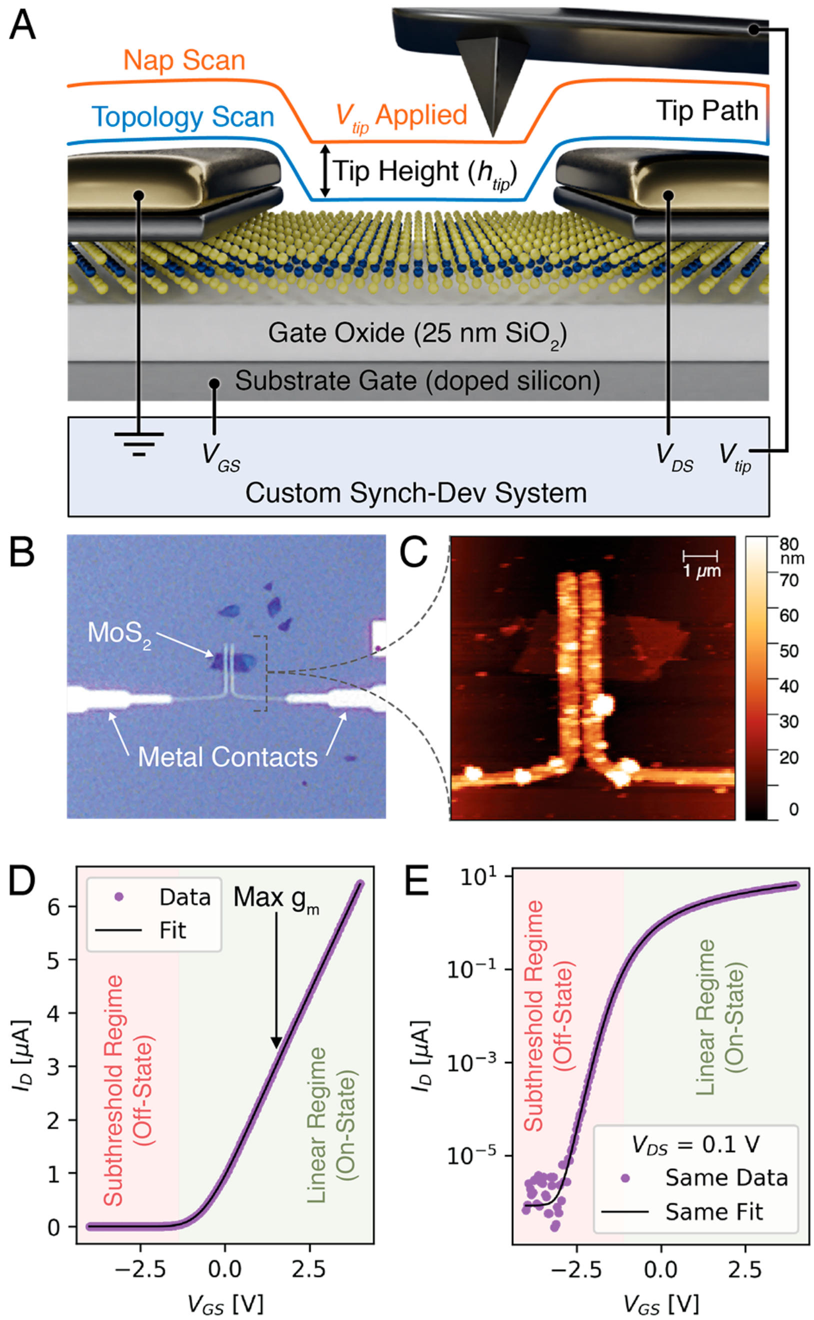

Figure 1. MoS_2 FET-based sensor structure, device operation, and SGM setup. (A) Schematic illustrating the SGM process, showing that a voltage is applied to an AFM tip to simulate a charged analyte while the tip is rastered at a fixed height above the FET being electrically characterized by a synchronized electrical device characterization setup (Synch-Dev). (B) An optical image showing Ni source/drain contacts (10 nm Ni/20 nm Pd) deposited onto an MoS_2 flake, forming a device. (C) An AFM scan showing the topology of a typical device. (D) Transfer and (E) subthreshold characteristics of an example MoS_2 FET (identical data and fit shown in each panel on linear and log scales, respectively).

sensors have been demonstrated, among many other applications, for prenatal genetic screening,[10] sensing antibiotic concentrations,[13] and detecting cancer biomarkers.[14]

Although 2D material-based sensors show great promise, considerable challenges remain, particularly related to consistent sensor operation, selectivity in real-world conditions, and device yield during manufacture. While the very nature of a 2D material with nearly all-surface charge transport provides sensitivity to electrical perturbations in its vicinity, the best practices to consistently transduce these perturbations remains elusive. Most demonstrations found in the literature occur in controlled environments or using one operational device out of many that were fabricated. Furthermore, the literature abounds with conflicting conclusions regarding key aspects of sensor operation, including the ideal operating point.

Most of these 2D material-based sensors are configured as field-effect transistors (FETs) in which the 2D material is used as the FET channel.[15] When designing and fabricating such a sensor a number of key design choices need to be made, including the optimal location of analyte sensing (at the source, at the drain, localized in the channel, spread across the channel, *etc.*), the thickness of the encapsulation layer(s), the

https://dx.doi.org/10.1021/acsnano.0c04192
ACS Nano 2020, 14, 11637−11647

FET polarity (*p*- or *n*-type), and the operating point—transistor off-state (subthreshold regime) or on-state (saturation or linear regime). These are only a few of the critical choices, which together comprise an expansive parameter space for determining the most appropriate sensor design. The difficulty of explicitly controlling many of these variables limits the feedback that could illuminate underlying mechanisms and guide rational design iterations. For instance, when testing a biosensor, it is typically not feasible to maintain control over the location of an analyte molecule relative to the sensing element with nanometer precision. However, the specific location of the analyte typically makes a significant difference in the detected signal. Without an understanding of the influence of key variables that affect the detection mechanisms, it is unlikely that 2D FETs will reach their full potential and realize broad adoption.

To address these shortcomings, we used a customized atomic force microscope (AFM) with a synchronized electrical device control platform (Synch-Dev) to explore the impact of precise analyte position and charge on signal transduction in a 2D FET-based sensor. The apex of the AFM cantilever tip acted as the analyte, with the tip voltage representing the effective analyte charge and the Synch-Dev providing synchronized electrical biasing of the FET and tip voltage. Utilizing this functionality, we explored the operation of an MoS_2 FET-based sensor and observed "hotspots" of sensitivity distributed throughout the channel, with no evident preference for the source-side or drain-side of the device. Through varying the height of the voltage probe, sensitivity to remote charges was characterized, showing substantial benefits to reducing the analyte−channel separation. Importantly, an increased sensitivity to local charge was observed when the charge gated the transistor toward the off-state rather than the on-state. Three distinct types of signal-to-noise ratio (SNR) were defined based on prior sensor demonstrations, and each of these was analyzed for efficacy in this controlled charge characterization setup. This analysis yielded evidence of the ideal range of operation for many sensing modalities, which is around the threshold voltage of the device and depends on the extent of the channel that is gated. These observations provide insight for the design of 2D FET-based sensors and the most appropriate operating mode for maximized SNR.

RESULTS AND DISCUSSION

The customized AFM setup used in this study was leveraged to perform several types of scanning probe microscopy (SPM), such as electrostatic force microscopy (EFM), Kelvin-probe force microscopy (KPFM), and scanning gate microscopy (SGM). These and other similar measurement methods have seen some use on 2D-FETs previously.[16] While EFM and KPFM are available with many traditional AFM instruments, our modified SGM approach required additional channels of synchronized measurements provided by a custom *in situ* FET characterization system (Synch-Dev), portions of which have been described previously.[17,18] This latter approach provided the most illuminating and pertinent data, enabling direct correlation between the SGM tip position and the charge with the MoS_2 FET behavior under active bias. Many reports have presented SGM on graphene devices,[19−22] mostly from the perspectives of observing insights stemming from graphene's band structure. To date, however, application of the SGM technique to other 2D materials has been limited. For MoS_2, SGM has been used to highlight electrical domain boundaries[23] and to suggest that electron beam exposure may lead to a phase transition.[24]

Although not traditionally used for this purpose, SGM is very well suited to physically simulate many aspects of FET sensing with high degrees of precision and control. To perform an SGM scan, a sharp tip is first scanned over the surface of a device, as in AFM. Once the end of the scanline is reached, the tip is raised by a preset distance (h_{tip}) and rescanned over the same line maintaining a constant height above the surface (Figure 1A). This second, raised line scan is referred to as the nap scan. During the nap scan, a voltage (V_{tip}) is applied to the tip while a substrate gate voltage (V_{GS}) and a device drain to source voltage (V_{DS}) are applied to the FET, setting the sensor operating point. The device's drain current (I_D) is then recorded during the nap scan and mapped to the position of the tip, thus forming an image.

The Synch-Dev system we developed in this work integrates several instruments and interfaces providing compelling capabilities. In this system, device chips are wire-bonded into packages which are in turn inserted into custom printed circuit boards (PCBs). These PCBs make the use of micromanipulators unnecessary and thus increase the stability of electrical measurements while other system components are in motion. Source measure units (SMUs) interface with these PCBs to provide stable voltage application and current measurement down to 10 fA. Furthermore, hardware triggering and communication bus paths were implemented between the AFM, four SMUs, the PCBs, and a control computer to provide tight synchronization between the measurements. Extensive software was developed and deployed at each system node to facilitate control, synchronization, automation, and data fusion. Further details of this system are outlined in the Supporting Information along with Figure S1.

The devices studied in this work were fabricated by forming metal contacts on exfoliated MoS_2 flakes (approximate thickness 5−10 nm) using electron beam lithography (EBL), metal evaporation, and a lift-off process. Channel lengths were 500 nm, with channel widths on the order of 1 μm (determined by the flake geometry). A doped silicon substrate was used as a device back gate with a 25 nm thermal SiO_2 gate oxide. Full fabrication details can be found in the Supporting Information. Typical optical and AFM images of the completed devices are shown in Figure 1B,C. These devices yielded on/off-current ratios of over 6 orders of magnitude with on-currents on the order of 10 μA at V_{DS} = 100 mV (see Figure 1D,E). These device characteristics are similar to many others currently reported in the literature, making the results presented here broadly applicable. Transfer and subthreshold characteristics of the several devices studied are shown in Figure S2.

Using the combination of these MoS_2 devices and our custom Synch-Dev measurement system, the response of a device was mapped across the in-plane location of the simulated analyte (charged tip). An example of this type of mapping is shown in Figure 2B, where the topography of the same device is shown in Figure 2A. The nature of the interaction between the tip and the channel was capacitive, with no measurable current flowing to or from the tip. It is clear that the sensitivity of the device to the simulated analyte varies across both the length and the width of the channel, with some regions showing a strong response to the presence of the tip while the response is minimal in other regions. As can be seen in Figure 2B, "hotspots" of sensitivity occur throughout

https://dx.doi.org/10.1021/acsnano.0c04192
ACS Nano 2020, 14, 11637−11647

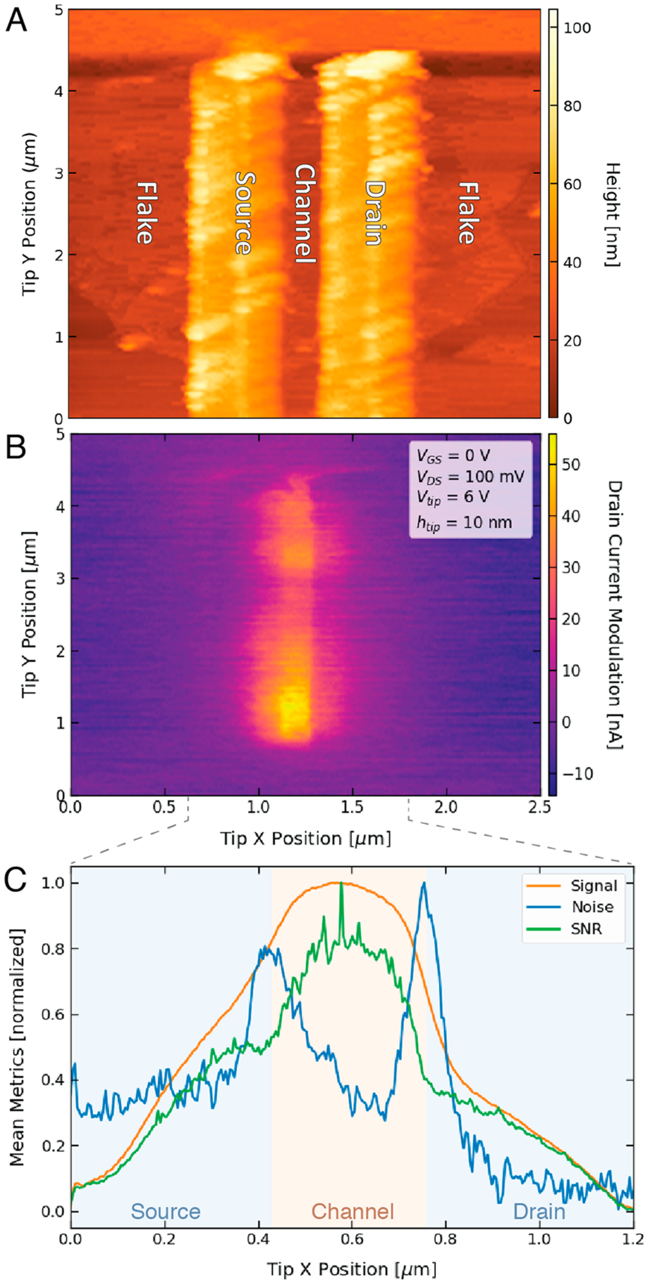

Figure 2. Sensitivity and hotspot identification across the MoS_2 channel. (A) Topology scan corresponding to parts (B) and (C). (B) "Hotspots" are shown in the nonuniformity of the device response to a controlled local charge. The modulation of the device drain current is shown versus the position of the local charge above the device, at a fixed height under the parameters listed in the inset (note: V_{GS} of 0 V is in the on-state for these transistors—see Figure 1D,E). (C) The normalized signal (drain−current modulation), noise (standard deviation from multiple repeated line scans), and SNR of an average scan line across the device (i.e., average of all scan lines), showing that both the signal and the SNR peak near the center of the channel, on average.

the channel. This observation is similar to results reported in other systems.[23,25] It has been proposed that these hotspots arise from defects,[26,27] inhomogeneities in the density of states,[28] charge irregularities in the substrate,[29,30] or differences in adhesion/contamination between the 2D material and the substrate.[31]

No systematic variation in the sensitivity across the channel geometry was observed here, such as increased sensitivity near one contact, as has been proposed previously.[23] Instead, the sensitive hotspots occurred randomly within the channel of the device. When the same device was scanned on different days and under different operating conditions, the locations of the hotspots remained constant, suggesting that they arise from a stable characteristic of either the channel, the substrate, or their interface. The presence of sensitivity hotspots was observed across many devices and operating conditions.

If these hotspots truly occur at random, it would be difficult to conceive of a sensor design that could take advantage of the higher sensitivity they offer. One valid approach to solve this issue could be to establish precisely what type of defect or contaminant leads to these hotspots and to determine if they can be reliably placed during fabrication. This route is recommended for future work; meanwhile, the focus herein lies on characterizing existing behavior. As such, we have worked to determine the most probable hotspot locations. By taking the average response of all line scans across a device's channel, the signal peak illustrates where, on average, the channel exhibits a maximal response (i.e., highest probable location of hotspots). An example of this type of line scan average is shown in Figure 2C, where it is clear that the device response, or signal, is maximized halfway between the source and the drain, on average.

When operating a sensor, maximizing the signal alone is typically not the primary objective. Instead, the signal-to-noise ratio (SNR) is often a more valuable metric, as it allows for the determination of what levels can be resolved independent of amplification. While mapping the response across a device has made it clear that hotspots exist that cause the generation of larger signals than other areas (see Figure 2B), these mappings have not given any indication of what contribution these hotspots may make to the observed noise levels. To determine what this contribution may be, our custom Synch-Dev measurement system was adjusted to allow for multiple measurements of the same line scan, allowing a noise metric to be extracted as the standard deviation of repeated measurements. This capability allows signal, noise, and SNR to be mapped with respect to each of the other system variables. The noise was found to rise along with the signal, but to a lesser extent, such that the SNR is maximized near the center of the channel length along with the signal (see Figure 2C). This implies that analyte wells or similar structures should be designed to expose analytes to the center of the channel to maximize SNR. It has been proposed that some sensors derive the majority of their sensitivity from the contacts or contact interface,[32,33] but this is not supported by the devices tested here.

In addition to determining the dependence of the sensor response on the lateral position of the simulated analyte, it is also valuable to measure the relationship between the sensor response and the out-of-plane distance of the analyte. Many 2D material-based charge detection sensors are likely to require a passivation layer to protect the sensitive material from degradation from either the environment or the analyte[9,34] (for example, 2D materials like black phosphorus are degraded by both oxygen and water[35]). Other sensors will require bioreceptors, linkers, or adhesion layers to attract or bind the intended analyte. Any such layer, whether intended for passivation or analyte binding, will increase the distance between the 2D material and the analyte. Although it is clear

https://dx.doi.org/10.1021/acsnano.0c04192
ACS Nano 2020, 14, 11637−11647

that sensitivity will decrease as the analyte is moved farther from the device channel, the utility or even necessity of interlayers motivates determination of the precise relationship between device response and analyte distance. This relationship can be used to evaluate trade-offs between interlayer thickness and sensitivity during the sensor design process.

To this end, SGM scans were taken across a range of heights. As expected, the device response was reduced and broadened as the out-of-plane distance to the simulated analyte was increased, as shown in the example scans in Figure 3A. Note that the lateral locations of the hotspots remained constant across analyte heights. To quantify the relationship encoded in this set of images, we defined a metric of device responsiveness; specifically, the 99th percentile of the device response across the scan image was used to capture the effective maximal response while avoiding susceptibility to potential outliers. We then extracted this metric from each image and plotted it against height in Figure 3B. More scan images and a more complete breakdown of percentiles are shown in Figure S3.

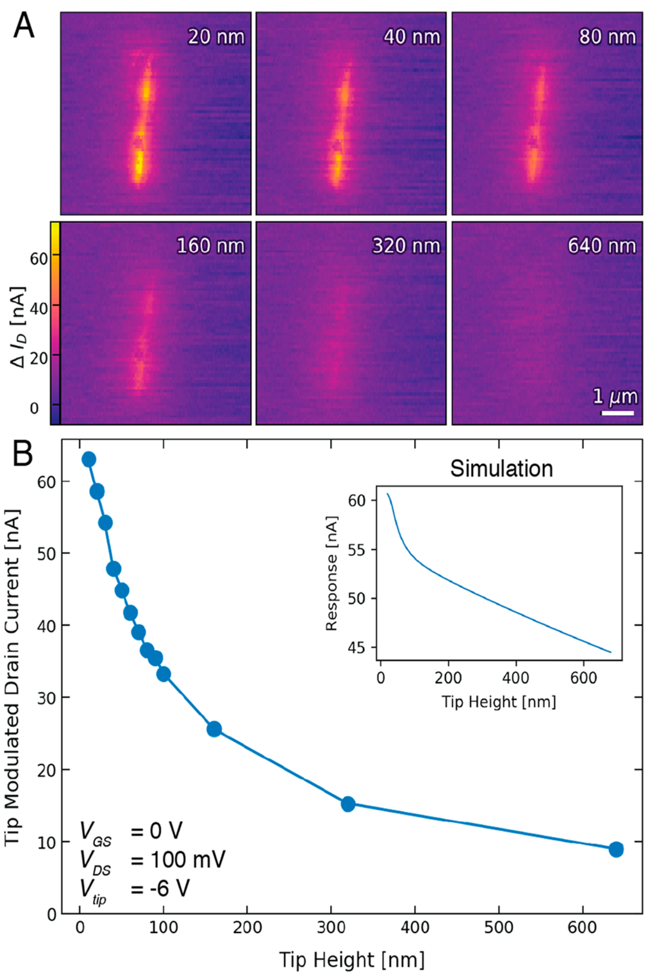

Figure 3. Dependence of the sensitivity on analyte height. (A) SGM maps showing the magnitude of the drain current modulation versus the location of the simulated analyte for a range of heights (indicated in the top right corner of each map). (B) Relationship between the device response and the analyte height is expressed by summarizing each full scan with a response metric (99th percentile of modulated drain current across the scan image), while the inset shows a similar trend predicted by our numerical model.

To further explore this trend, we developed a model in which a device channel was represented as a transistor mesh grid, with the gating of each node calculated from a geometrical electrostatics model, as described in the Supporting Information (see also Figures S4−S6). This model accurately reproduced the qualitative shape of the device response as a function of tip height for small distances; however, at larger distances, it predicted that the response would drop off more slowly with distance than was observed (see Figure 3B). The qualitative similarity between the model predictions and our observations provides some validation of the data collection and analysis methodology. The assumptions of the model are general to all FET-based charge detection sensors, suggesting that the observed trend may be generalizable beyond the specific devices and materials used in this study. We were surprised how steeply the response declined within the first 100 nm, even without the large amount of charge screening present in some sensors. This fast decay in sensitivity with distance highlights the need for developing ultrathin capping layers,[36] short linker molecules, aptamers to replace antibodies,[37] polymer brush layers allowing use of the Donnan effect,[38] and other methodologies that enable smaller distances between the device channel and the analyte.

Although the majority of the details of our numerical model are specific to localized charge detection and are described primarily in the Supporting Information, our general FET model is more broadly applicable and will be briefly summarized here. This model was adapted from previous work[39,40] to provide a single equation with no conditionals that is valid, continuous, and differentiable across all operating regimes. Furthermore, this model is defined in terms of common device performance metrics, so that it can be easily used by experimenters to extract performance metrics from a typical device or be fit to data in order to obtain estimates and estimate uncertainties for key parameters that are commonly reported. In this model, the FET drain current (I_D) is given by

$$I_D = 2\left(\frac{nk_BT}{q}\right)^2 \frac{g_m}{V_{DS}}({q_{is}}^2 - {q_{id}}^2)$$

where $q_{is} = W[e^{q(V_{GS}-V_T)/2nk_BT}]$, $q_{id} = W[e^{q(V_{GS}-V_T-V_{DS})/2nk_BT}]$, $n = \frac{q}{k_BT}\frac{SS}{\ln(10)}$, k_B is Boltzmann's constant, T is the temperature in kelvin, q is the charge of an electron, g_m is the device transconductance, V_{DS} is the device drain voltage, W is the lambert W function (real part, available in most scientific computing packages, can also be globally approximated in terms of logrithms,[41] with arguments shown in square brackets), V_{GS} is the device gate voltage, V_T is the device threshold voltage, and SS is the device subthreshold swing in volts/decade. A fit of this model to example device data is shown in Figure 1D,E. A series of plots demonstrating the model outputs across a range of input device metrics is shown in Figure S4, alongside an expanded version of the model including mobility degradation. This model can be easily used to extract device metrics from current versus voltage data or to model the effect of device metrics on observed results, as in our expanded sensor numerical model.

In sensing applications, it is typically quite difficult to make a change to the charge of the analyte to determine what effect the magnitude of that charge entails. The few studies that have

https://dx.doi.org/10.1021/acsnano.0c04192
ACS Nano 2020, 14, 11637−11647

managed to vary this parameter for specific sensors had to use impressive experimental feats to do so.[42] Here, however, our experimental system allows precise control over the analyte charge, which enables us to determine the influence of both the magnitude and the polarity of the charge. To this end, full SGM scans were taken across a range of tip voltages with repeated measurements to enable extraction of a noise metric (the standard deviation of the multiple measurements). As discussed previously, the magnitude of both the response and the noise were extracted from each scan. This allowed an SNR value to be calculated from each scan image. We found that the system noise was not significantly affected by the analyte charge, suggesting that the SNR was governed by the signal.

Although, as expected, the SNR increased with the magnitude of the analyte charge, we found that the SNR increased more rapidly when the charge was acting to turn the FET to the off-state compared to the on-state (Figure 4A). This may seem counterintuitive, since the slope of the FET transfer curve is increasing with gate voltage over the majority

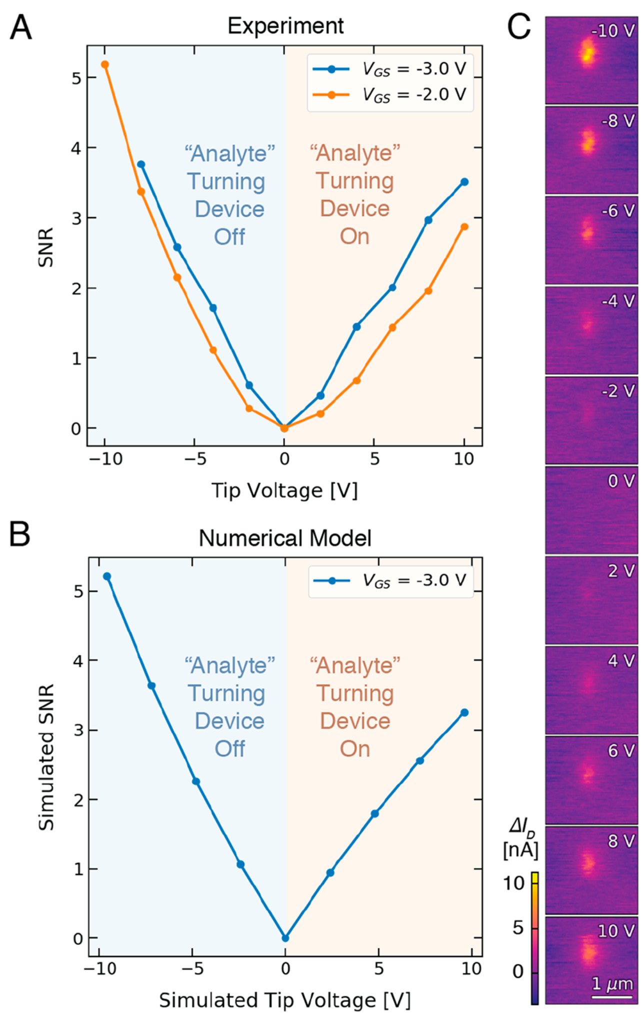

Figure 4. SNR is asymmetrically influenced by analyte charge polarity. (A) SNR dependence on the tip (simulated analyte) voltage, revealing a stronger increase when the analyte acts to turn the FET off; the behavior is consistent for two different operating points. (B) Numerical model predicting the same asymmetry that was experimentally observed. (C) Example SGM scans that were summarized in (A) shown for reference with their associated tip voltages (V_{tip}) indicated in the top right corner of each scan.

of the operating range, such that gating perturbations pushing the device further into the on-state may be expected to increase the drain current slightly more than perturbations pushing it toward the off-state. This argument would not hold if the operating point set by the substrate gate were far enough into the on-state to set the device past the point of maximal transconductance, but we observed the same trend at multiple operating points, all on the subthreshold side of maximal transconductance. Since these devices experience some hysteresis, the scan through tip voltages was completed in the direction that would minimize the observed asymmetry, such that the asymmetry would have been larger should the progression of tip voltages proceeded in the opposite direction.

It could be argued that when the device is held near the threshold voltage (i.e., transition voltage between the off- and on-states), gating perturbations would encounter an exponential relationship toward the off-state and a linear relationship toward the on-state (see the log-scale subthreshold curve in Figure 1E), explaining the observed asymmetry in the response. This argument, however, does not hold because the slope of the exponential relationship is everywhere lower than the slope of the linear relationship (see Figure 1D). Since the signal is defined as an absolute change in drain current rather than a percentage change in drain current, it is the slope of the drain current versus gate voltage relationship that should determine the result. Additionally, the fact that this trend was exhibited at multiple operating points (Figure 4A) demonstrates that it is not specific to operating at or near the threshold voltage.

Because the two lines of reasoning just presented do not appear to explain the observed results, the numerical model discussed above (i.e., using a 2D mesh grid of transistors to represent the FET channel) was employed to discover the root cause of the measured asymmetry. The predictions of this model were in good agreement to the measurements, as shown in Figure 4B. The modeling process helped to illuminate an underlying reason for the asymmetric response with simulated analyte polarity: the analyte effectively perturbs the conductance of a segment of the channel. For small perturbations, the magnitude of a positive conductance perturbation will be similar to that of a negative perturbation. In a model as simple as a chain of three resistors, if the conductance of any single resistor is decreased by 50% or increased by 50%, the overall conductance of the chain will change by −25% or +12.5%, respectively (see Figure S7). The numerical mesh model, although much more sophisticated, follows roughly the same principle as the mental model of the three-resistor chain. Both models indicate that a local disruption in current (decrease in conductance) leads to a larger global impact on current flow across the channel than an equal and opposite local enhancement (increase in conductance).

With this underlying mechanism identified, it is reasonable to project that the asymmetry between response to a positive analyte charge versus response to a negative analyte charge is a result that is generalizable to all types of FET-based sensors in similar configurations. The mechanism discussed is not specific to a certain operating point or operating range, nor is it specific to MoS_2 or even 2D materials. With all else equal, a FET-based charge sensor where the analyte modulates the device toward its off-state will have a higher SNR than the same sensor where an analyte of the opposite charge modulates toward the on-state. As such, we recommend that, when designing a FET-based sensor to detect a charge-based analyte, a device be

https://dx.doi.org/10.1021/acsnano.0c04192
ACS Nano 2020, 14, 11637−11647

selected with a polarity such that it will be turned off by that analyte.

The next item to be determined for FET-based sensors is the ideal operating point, i.e., the operating point at which the SNR is maximized. There has been some debate in the literature as to where the ideal operating point may be, with some studies suggesting that it will occur at the point of maximum transconductance[43] (in the center of the linear regime), while others concluded that this point is in the subthreshold regime.[44] The discrepancy between the conclusions of these studies suggests that more work is needed to resolve the issue.

To that end, we performed SGM scans on our devices accounting, as before, for both signal and noise estimation across a range of substrate gate voltages (i.e., operating points). One SNR value was extracted from each full scan image, with three full scans performed at each gate voltage in order to obtain a measurement of uncertainty (standard deviation). Figure 5C shows that the SNR peaks are located consistently near the center of the subthreshold regime. This trend was observed to hold true for measurements across multiple devices as well as for multiple measurements of the same device. An effective transfer curve and transconductance relationship were each extracted from the same set of scan images and are shown aligned to the same axis in Figure 5A,B, illustrating that the SNR peak is far removed from the transconductance peak. The transconductance peak is located in the center of the on-state, whereas the SNR peak is in the center of the off-state.

This operating point experiment was repeated for both a positive and a negative analyte charge (AFM tip charge), with the location of the SNR peak remaining in the off-state for both charge polarities (Figure 5C). The SNR peaked at a slightly higher gate voltage when the analyte was turning the device off, as predicted by our numerical model (Figure S8). As indicated earlier, the SNR is higher when the analyte charge was pulling the device toward the off-state than when it was pulling the device toward the on-state. At some operating points, the difference between SNRs with a positive compared to negative analyte charge was small; however, this difference was exaggerated near the SNR peak. The peak SNR with the device being turned more off by the analyte was roughly three times larger than the peak SNR with the device being turned on by the analyte. This reinforces our earlier recommendation of choosing a device polarity that will be turned off by the intended analyte when designing a sensor. Interestingly, a crossover in this trend was observed far into the on-state (see Figure 5C near V_{GS} = 1 V), but in this region the difference between the SNRs for the opposite analyte charges was small. Figures 4 and 5 provide four cross sections through the SNR *versus* V_{tip} and V_{GS} surface, illustrating the rough trends observed across these parameters.

Across the range of operating points studied, the noise rose with increasing device drain current, independent of analyte charge polarity. The shape of the signal with respect to the operating point, however, was markedly different between the two polarities. The breakdown of the SNR into signal and noise components is shown in Figure 5D−E. Note that the noise observed in these devices was found to be predominantly flicker noise, due to the low measurement frequencies utilized in the experiments.

We performed two distinct versions of this experiment, with both leading to very similar results. In the first version (results shown in Figure 5), the voltage difference between the tip and the gate ($V_{TG} = V_{tip} - V_{GS}$) was held constant as the gate voltage was varied. This was done to maintain the magnitude of the gating modulation through the tip at a constant value around the global operating point. In the second version of the experiment (results shown in Figure S9), the tip voltage (V_{tip}) was held at a constant value as the gate voltage was varied.

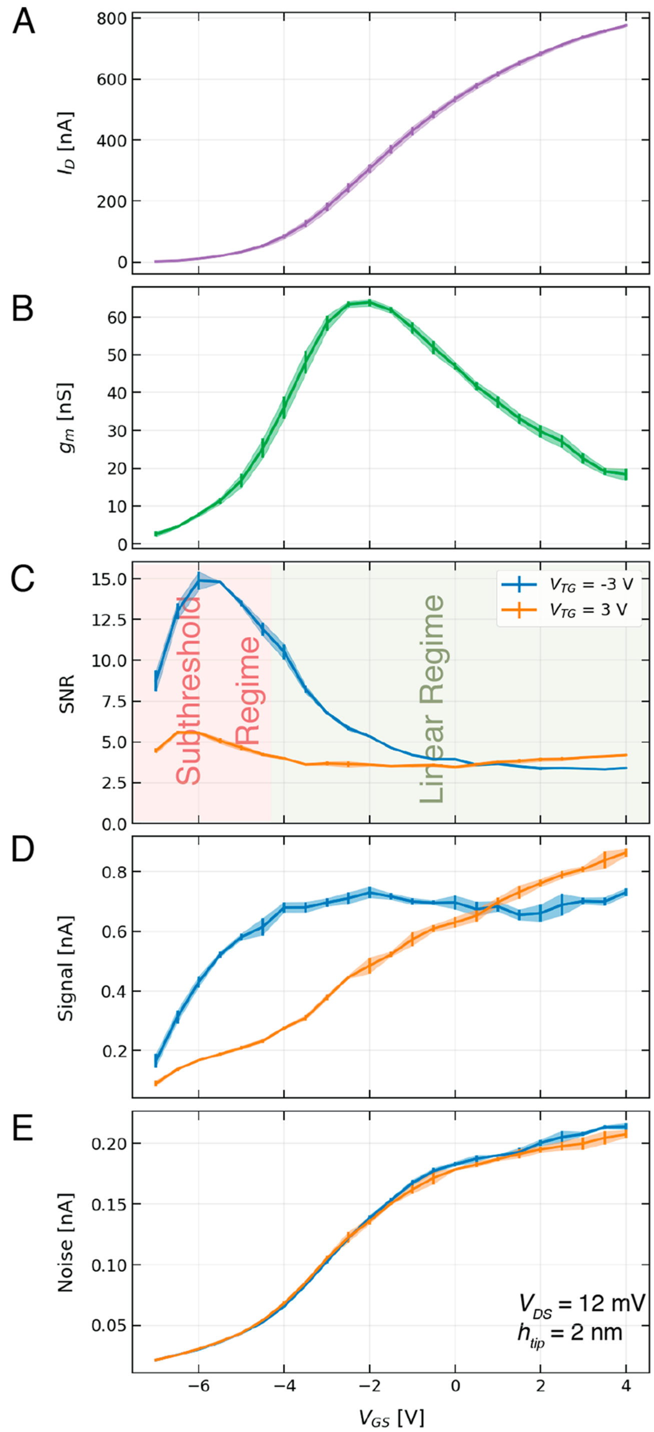

Figure 5. Influence of the operating point on the SNR, showing the max in the subthreshold regime. The results from a large number of SGM scans of a MoS_2 FET are summarized in terms of (A) drain current, (B) transconductance, (C) SNR, (D) signal, and (E) noise across a range of operating points and for two analyte polarities ($V_{TG} = V_{tip} - V_{GS}$).

https://dx.doi.org/10.1021/acsnano.0c04192
ACS Nano 2020, 14, 11637−11647

Both versions (varying V_{TG} in one and V_{tip} in the other) were repeated for a positive and a negative effective analyte influence. Results from each version showed SNR peaking in the subthreshold regime, with the analyte influence that modulates the device toward its off-state leading to a much higher maximal SNR.

Up to this point, the signal of our sensor has been defined to be the maximum change in current through the device seen in response to our voltage probe (i.e., the maximum color change seen in a scan image). The SNR can be defined in terms of three distinct signal metrics. For FET-based sensors these three signal types are often expressed as conductance (G), change in conductance when the analyte is introduced (ΔG), and percentage change in conductance when the analyte is introduced ($\Delta G/G$). There are distinct use cases associated with each of these signal metrics that illustrate the role and importance of each. If the analyte has full control over the gating of the device (although this is rarely the case), then G alone would be appropriate. If the analyte causes small perturbations in the gating of the channel, which is centered around an operating point set by another gate (such as a back gate), then ΔG would be an appropriate signal metric when no amplifier is used. When an amplifier is used, however, the absolute size of ΔG becomes less important, as percentage changes can be amplified to a different absolute scale. In this case $\Delta G/G$ (or a percentage change) becomes the most useful signal metric. Note that the choice between ΔG and $\Delta G/G$ could depend on the specifics of the measurement and amplification approach, as some approaches lend themselves more easily to rereferencing than others. Since ΔG is a very common signal metric, use of the terms signal and SNR in this work refer to the ΔG definition of the signal, unless otherwise specified.

An SNR can be derived from each of these types of signals, and the ideal operating point depends heavily on the appropriate SNR for the sensor setup in question. To illustrate the difference between the three SNRs derived from these three signal metrics, we performed substrate-gated measurements of our MoS_2 devices, with noise calculated from the variation of 50 000 measurements under the same conditions. Three SNRs have been calculated from the results using the three definitions discussed above and are shown in Figure 6 plotted as a function of the operating point. When gating perturbations affect the entire channel via the substrate gate, SNR_G increases steadily throughout the on-state, $SNR_{\Delta G}$ peaks slightly to the subthreshold side of peak transconductance, and $SNR_{\Delta G/G}$ has a peak deep in the subthreshold regime.

Using the same device, we have shown that gating perturbations that affect the entire channel lead to a $SNR_{\Delta G}$ peak near the point of maximum transconductance (Figure 6), whereas gating perturbations that affect a localized region of the channel lead to a $SNR_{\Delta G}$ peak centered in the subthreshold region (Figure 5C). This apparent behavioral difference provides insight regarding the disagreement in the literature about where this SNR peak will be found. Our numerical model predicts that if the analyte influence were to span the entire channel, the $SNR_{\Delta G}$ peak would shift toward the on-state as compared to when the analyte influence is localized to a small area of the channel (Figure S10). The predicted shift is not as large as the experimentally observed shift (experimental shift observed from the peak position difference of Figure 6 versus Figure 5C). We surmise that this difference is likely a result of how the model predicts noise by assuming that it is a

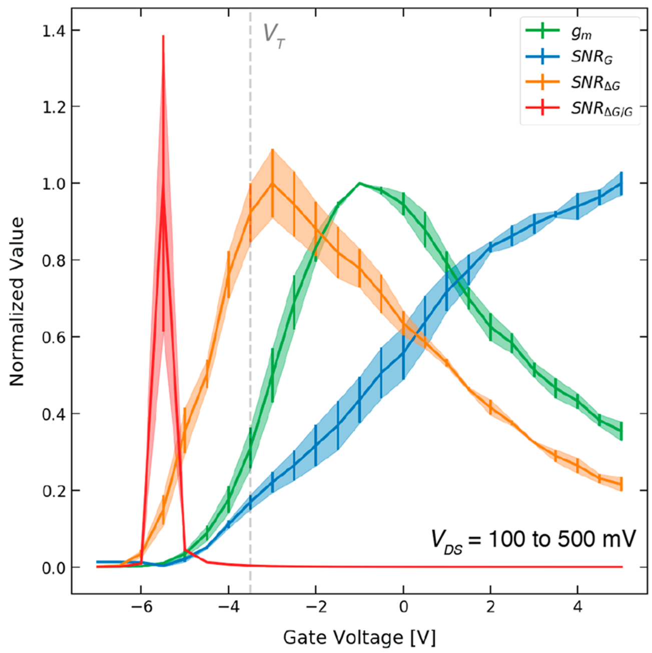

Figure 6. Types of SNR and their dependence on the operating point for global gating. Three different types of SNR (see text) are plotted as a function of the gate voltage (operating point). The data illustrate that the SNR most pertinent to a given sensor will have bearing on its ideal operating point. These global gating measurements were performed on the same device as the local gating measurements presented in Figure 5, allowing comparison of the SNR peak positions relative to peak g_m. The error bars were computed as ± 1 standard deviation of measurements across drain voltages ranging from 100 mV to 500 mV, indicating that the shapes of these normalized trends are independent of drain voltage over the range studied. The transconductance and threshold voltage are shown for reference.

constant percentage of the drain current in both instances. While our data confirms that this assumption is approximately accurate for the case of localized gating perturbations, our global gating perturbation measurements clearly indicate that this assumption is not valid in that case. It has also been previously proposed that changes near the contacts could influence the extent of gating and may alter the noise profile.[43]

When moving from a global to a local analyte influence, our model predicts that changes in the signal will push the $SNR_{\Delta G}$ peak toward subthreshold. Furthermore, our noise measurements indicate that changes in the noise profile will push the $SNR_{\Delta G}$ peak toward subthreshold, and our $SNR_{\Delta G}$ peak measurements confirm that this peak shifts from near the transconductance peak for a globally gated device (Figure 6) to the center of the subthreshold regime for a local-analyte-gated device (Figure 5C). Future work should include the observation of intermediate steps of this shift by creating localized influences of various extents. This could be achieved by creating analyte exposure wells of several sizes on similar channels.

The observation that the location of the SNR peak is dependent on the portion of the channel that is influenced by the analyte has important implications for many sensors. Some FET-based sensors require contact passivation,[45,46] and this passivation layer most often extends over a portion of the channel, causing only a part of the channel to interact with the analyte. Other sensors have discrete wells formed on the device

https://dx.doi.org/10.1021/acsnano.0c04192
ACS Nano 2020, 14, 11637−11647

channel and only allow the analyte to interact with the channel inside these wells.[47] Some sensors expose the entire channel to the analyte,[48] while still other sensors detect single molecular events that only influence a small portion of the channel at any given time.[49] The SNR in each of these schemes will likely be influenced according to the principles discovered here and outlined above.

Some care will be required in extending the results presented in this work to specific sensor designs. For instance, since this work did not include a dielectric passivation layer covering the active area of the FET channel in either the experiments or the numerical model, a sensor that uses such a layer would require the adjustment of all trends versus analyte distance by considering the appropriate dielectric constants and layer thicknesses. Similarly, the functionalization of the channel to enhance sensitivity would lead to a threshold voltage shift if the functionalization layer is charged and changes in transconductance if the layer introduces scattering sites. Such changes in device performance metrics could be adjusted in the inputs to the numerical model presented here in order to gain an approximate understanding of what influence they may enact. When this type of care and consideration are taken, the principles defined and characterized in this work remain highly relevant and are applicable guidelines for future sensor development.

CONCLUSIONS

Our custom measurement system allowed us to investigate a highly controlled sensor based on a 2D FET, exploring the effects of parameters that are difficult to control in typical sensors of this type. Our results show that a device is not uniformly sensitive across the channel, but rather the device exhibits sensitivity "hotspots", with locations that remain stable in time. On average, however, the SNR is maximized near the center of the channel, suggesting that analyte wells should be placed there in practice. We found that the response of the device is highly asymmetric with respect to the polarity of the analyte charge—an analyte that turns the device off leads to higher SNRs, and we identified a broadly applicable mechanism for this effect. This suggests that device polarity should be chosen such that the device will be gated toward the off-state by the analyte of interest. This asymmetry is most strongly manifest at the operating point that leads to maximal SNR, which we determined to be in the subthreshold regime when the device is locally gated. The ideal operating point in terms of SNR, however, was found to shift with the extent of the channel that was gated, with our numerical model suggesting this may be a continuous shift as the extent of gating is varied. Verification of this proposed continuous shift in the ideal operating point with extent of gating would be a valuable subject in future work. Our findings, along with a clear definition of different types of SNR and when each should be used provide a clear pathway for designing 2D material FET-based sensors.

METHODS

The devices were fabricated from mechanically exfoliated MoS_2 flakes that were transferred to a *p*-type silicon wafer with 25 nm thermal oxide with a grid of palladium interconnects previously formed via photolithography, electron-beam evaporation, and liftoff. Thin flakes were selected for device fabrication using an optical microscope based on the contrast of the flake with the substrate. The nickel source and drain contacts were formed by electron-beam lithography of the PMMA resist, electron-beam metal evaporation, and lift-off. Chips were wire-bonded into 68 pin ceramic packages, which were inserted into our custom designed PCBs to be measured by our Synch-Dev system developed for this work. Further specific details of the fabrication process, the measurement system, and the numerical models referred to throughout the text are described in the Supporting Information.

ASSOCIATED CONTENT

Supporting Information

The Supporting Information is available free of charge at https://pubs.acs.org/doi/10.1021/acsnano.0c04192.

Figures S1−S10 and further details regarding fabrication, the measurement system, and the numerical model (PDF)

AUTHOR INFORMATION

Corresponding Author

Aaron D. Franklin − *Department of Chemistry and Department of Electrical & Computer Engineering, Duke University, Durham, North Carolina 27708, United States*; orcid.org/0000-0002-1128-9327; Email: aaron.franklin@duke.edu

Authors

Steven G. Noyce − *Department of Electrical & Computer Engineering, Duke University, Durham, North Carolina 27708, United States*; orcid.org/0000-0002-2953-7560

James L. Doherty − *Department of Electrical & Computer Engineering, Duke University, Durham, North Carolina 27708, United States*; orcid.org/0000-0003-1571-0622

Stefan Zauscher − *Department of Mechanical Engineering and Materials Science, Duke University, Durham, North Carolina 27708, United States*; orcid.org/0000-0002-2290-7178

Complete contact information is available at: https://pubs.acs.org/10.1021/acsnano.0c04192

Author Contributions

S.G.N. and A.D.F. designed the experiments. S.G.N. performed experimentation and data analysis with feedback from the other authors. J.L.D. fabricated the devices and assisted in some experimentation. The manuscript was first drafted by S.G.N. and then refined through contributions of all authors. All authors have given approval to the final version of the manuscript.

Notes

The authors declare no competing financial interest.

ACKNOWLEDGMENTS

This work was supported by funding from the National Institutes of Health (NIH) under Award 1R01HL146849. This work was performed in part at the Duke University Shared Materials Instrumentation Facility (SMIF), a member of the North Carolina Research Triangle Nanotechnology Network (RTNN), which is supported by the National Science Foundation (Grant ECCS-1542015) as part of the National Nanotechnology Coordinated Infrastructure (NNCI).

REFERENCES

(1) Wen, W.; Song, Y.; Yan, X.; Zhu, C.; Du, D.; Wang, S.; Asiri, A. M.; Lin, Y. Recent Advances in Emerging 2D Nanomaterials for Biosensing and Bioimaging Applications. *Mater. Today* **2018**, *21*, 164−177.

(2) Schedin, F.; Geim, A. K.; Morozov, S. V.; Hill, E. W.; Blake, P.; Katsnelson, M. I.; Novoselov, K. S. Detection of Individual Gas Molecules Adsorbed on Graphene. *Nat. Mater.* **2007**, *6*, 652−655.

(3) Nasri, B.; Wu, T.; Alharbi, A.; You, K. D.; Gupta, M.; Sebastian, S. P.; Kiani, R.; Shahrjerdi, D. Hybrid CMOS-Graphene Sensor Array for Subsecond Dopamine Detection. *IEEE Trans. Biomed. Circuits Syst.* **2017**, *11*, 1192−1203.

(4) Zheng, Y.; Huang, L.; Zhang, Z.; Jiang, J.; Wang, K.; Peng, L. M.; Yu, G. Sensitivity Enhancement of Graphene Hall Sensors Modified by Single-Molecule Magnets at Room Temperature. *RSC Adv.* **2017**, *7*, 1776−1781.

(5) Fusco, L.; Gazzi, A.; Peng, G.; Shin, Y.; Vranic, S.; Bedognetti, D.; Vitale, F.; Yilmazer, A.; Feng, X.; Fadeel, B.; Casiraghi, C.; Delogu, L. Graphene and Other 2D Materials: A Multidisciplinary Analysis to Uncover the Hidden Potential as Cancer Theranostics. *Theranostics* **2020**, *10*, 5435−5488.

(6) Deen, D. A.; Olson, E. J.; Ebrish, M. A.; Koester, S. J. Graphene-Based Quantum Capacitance Wireless Vapor Sensors. *IEEE Sens. J.* **2014**, *14*, 1459−1466.

(7) Yang, A.; Wang, D.; Wang, X.; Zhang, D.; Koratkar, N.; Rong, M. Recent Advances in Phosphorene as a Sensing Material. *Nano Today* **2018**, *20*, 13−32.

(8) Wang, D.; Yang, A.; Lan, T.; Fan, C.; Pan, J.; Liu, Z.; Chu, J.; Yuan, H.; Wang, X.; Rong, M.; Koratkar, N. Tellurene Based Chemical Sensor. *J. Mater. Chem. A* **2019**, *7*, 26326.

(9) Sarkar, D.; Liu, W.; Xie, X.; Anselmo, A. C.; Mitragotri, S.; Banerjee, K. MoS_2 Field-Effect Transistor for Next-Generation Label-Free Biosensors. *ACS Nano* **2014**, *8*, 3992−4003.

(10) Liu, J.; Chen, X.; Wang, Q.; Xiao, M.; Zhong, D.; Sun, W.; Zhang, G.; Zhang, Z. Ultrasensitive Monolayer MoS_2 Field-Effect Transistor Based DNA Sensors for Screening of Down Syndrome. *Nano Lett.* **2019**, *19*, 1437−1444.

(11) Campos, R.; Borme, J.; Guerreiro, J. R.; Machado, G.; Cerqueira, M. F.; Petrovykh, D. Y.; Alpuim, P. Attomolar Label-Free Detection of Dna Hybridization with Electrolyte-Gated Graphene Field-Effect Transistors. *ACS Sensors* **2019**, *4*, 286−293.

(12) Nazemi, H.; Joseph, A.; Park, J.; Emadi, A. Advanced Micro- and Nano-Gas Sensor Technology: A Review. *Sensors* **2019**, *19*, 1285.

(13) Chen, X.; Hao, S.; Zong, B.; Liu, C.; Mao, S. Ultraselective Antibiotic Sensing with Complementary Strand DNA Assisted Aptamer/MoS_2 Field-Effect Transistors. *Biosens. Bioelectron.* **2019**, *145*, 111711.

(14) Soni, A.; Pandey, C. M.; Pandey, M. K.; Sumana, G. Highly Efficient Polyaniline-MoS_2 Hybrid Nanostructures Based Biosensor for Cancer Biomarker Detection. *Anal. Chim. Acta* **2019**, *1055*, 26−35.

(15) Wang, L.; Wang, Y.; Wong, J. I.; Palacios, T.; Kong, J.; Yang, H. Y. Functionalized MoS_2 Nanosheet-Based Field-Effect Biosensor for Label-Free Sensitive Detection of Cancer Marker Proteins in Solution. *Small* **2014**, *10*, 1101−1105.

(16) Wu, D.; Li, W.; Rai, A.; Wu, X.; Movva, H. C. P.; Yogeesh, M. N.; Chu, Z.; Banerjee, S. K.; Akinwande, D.; Lai, K. Visualization of Local Conductance in MoS_2 /WSe_2 Heterostructure Transistors. *Nano Lett.* **2019**, *19*, 1976−1981.

(17) Noyce, S. G.; Doherty, J. L.; Cheng, Z.; Han, H.; Bowen, S.; Franklin, A. D. Electronic Stability of Carbon Nanotube Transistors under Long-Term Bias Stress. *Nano Lett.* **2019**, *19*, 1460−1466.

(18) Doherty, J. L.; Noyce, S. G.; Cheng, Z.; Abuzaid, H.; Franklin, A. D. Capping Layers to Improve the Electrical Stress Stability of MoS_2 Transistors. *ACS Appl. Mater. Interfaces* **2020**, *12*, 35698.

(19) Bhandari, S.; Westervelt, R. M. Imaging Electron Motion in Graphene. *Semicond. Sci. Technol.* **2017**, *32*, 024001.

(20) Pascher, N.; Bischoff, D.; Ihn, T.; Ensslin, K. Scanning Gate Microscopy on a Graphene Nanoribbon. *Appl. Phys. Lett.* **2012**, *101*, 063101.

(21) Morikawa, S.; Dou, Z.; Wang, S. W.; Smith, C. G.; Watanabe, K.; Taniguchi, T.; Masubuchi, S.; Machida, T.; Connolly, M. R. Imaging Ballistic Carrier Trajectories in Graphene Using Scanning Gate Microscopy. *Appl. Phys. Lett.* **2015**, *107*, 243102.

(22) Herbschleb, E. D.; Puddy, R. K.; Marconcini, P.; Griffiths, J. P.; Jones, G. A. C.; Macucci, M.; Smith, C. G.; Connolly, M. R. Direct Imaging of Coherent Quantum Transport in Graphene *P-n-p* Junctions. *Phys. Rev. B: Condens. Matter Mater. Phys.* **2015**, *92*, 125414.

(23) Matsunaga, M.; Higuchi, A.; He, G.; Bird, J. P.; Ochiai, Y.; Aoki, N. Imaging Local Transport Property within MoS_2 Transistors by Scanning Gate Microscopy. In *2016 Compound Semiconductor Week, CSW*, Toyama, Japan, 26−30 June 2016; Institute of Electrical and Electronics Engineers Inc.: 2016.

(24) Baidoo, J.; Matsunaga, M.; Higuchi, A.; Yamanaka, T.; Ochiai, Y.; Bird, J. P.; Aoki, N.; Gong, Y.; Zhang, X.; Vajtai, R.; Ajayan, P. Field-Effect Characterization of Polymorphic Molybdenum Disulfide Using Scanning Probe Techniques. Presented at NanoJapan, Rice University, 2015. https://nanojapan.rice.edu/Downloads/2015%20SCI/Baidoo,%20Jacqueline_Abstract_Poster.pdf (accessed August 8, 2020).

(25) Connolly, M. R.; Puddy, R. K.; Logoteta, D.; Marconcini, P.; Roy, M.; Griffiths, J. P.; Jones, G. A. C.; Maksym, P. A.; MacUcci, M.; Smith, C. G. Unraveling Quantum Hall Breakdown in Bilayer Graphene with Scanning Gate Microscopy. *Nano Lett.* **2012**, *12*, 5448−5454.

(26) Bampoulis, P.; Van Bremen, R.; Yao, Q.; Poelsema, B.; Zandvliet, H. J. W.; Sotthewes, K. Defect Dominated Charge Transport and Fermi Level Pinning in MoS_2/Metal Contacts. *ACS Appl. Mater. Interfaces* **2017**, *9*, 19278−19286.

(27) Qiu, H.; Xu, T.; Wang, Z.; Ren, W.; Nan, H.; Ni, Z.; Chen, Q.; Yuan, S.; Miao, F.; Song, F.; Long, G.; Shi, Y.; Sun, L.; Wang, J.; Wang, X. Hopping Transport through Defect-Induced Localized States in Molybdenum Disulphide. *Nat. Commun.* **2013**, *4*, 2642.

(28) Chen, X.; Wu, Z.; Xu, S.; Wang, L.; Huang, R.; Han, Y.; Ye, W.; Xiong, W.; Han, T.; Long, G.; Wang, Y.; He, Y.; Cai, Y.; Sheng, P.; Wang, N. Probing the Electron States and Metal-Insulator Transition Mechanisms in Molybdenum Disulphide Vertical Heterostructures. *Nat. Commun.* **2015**, *6*, 6088.

(29) Zhang, Y.; Brar, V. W.; Girit, C.; Zettl, A.; Crommie, M. F. Origin of Spatial Charge Inhomogeneity in Graphene. *Nat. Phys.* **2009**, *5*, 722−726.

(30) Guo, Y.; Wei, X.; Shu, J.; Liu, B.; Yin, J.; Guan, C.; Han, Y.; Gao, S.; Chen, Q. Charge Trapping at the MoS_2-SiO_2 Interface and Its Effects on the Characteristics of MoS_2 Metal-Oxide-Semiconductor Field Effect Transistors. *Appl. Phys. Lett.* **2015**, *106*, 103109.

(31) Rosenberger, M. R.; Chuang, H. J.; McCreary, K. M.; Hanbicki, A. T.; Sivaram, S. V.; Jonker, B. T. Nano-"Squeegee" for the Creation of Clean 2D Material Interfaces. *ACS Appl. Mater. Interfaces* **2018**, *10*, 10379−10387.

(32) Hu, Y.; Zhou, J.; Yeh, P. H.; Li, Z.; Wei, T. Y.; Wang, Z. L. Supersensitive, Fast-Response Nanowire Sensors by Using Schottky Contacts. *Adv. Mater.* **2010**, *22*, 3327−3332.

(33) Zhang, J.; Boyd, A.; Tselev, A.; Paranjape, M.; Barbara, P. Mechanism of NO_2 Detection in Carbon Nanotube Field Effect Transistor Chemical Sensors. *Appl. Phys. Lett.* **2006**, *88*, 123112.

(34) Liu, G.; Rumyantsev, S. L.; Jiang, C.; Shur, M. S.; Balandin, A. A. Selective Gas Sensing with H-BN Capped MoS_2 Heterostructure Thin-Film Transistors. *IEEE Electron Device Lett.* **2015**, *36*, 1202−1204.

(35) Island, J. O.; Steele, G. A.; Van Der Zant, H. S. J.; Castellanos-Gomez, A. Environmental Instability of Few-Layer Black Phosphorus. *2D Mater.* **2015**, *2*, 011002.

(36) Price, K. M.; Schauble, K. E.; McGuire, F. A.; Farmer, D. B.; Franklin, A. D. Uniform Growth of Sub-5-Nanometer High-κ Dielectrics on MoS_2 Using Plasma-Enhanced Atomic Layer Deposition. *ACS Appl. Mater. Interfaces* **2017**, *9*, 23072−23080.

(37) Mukherjee, S.; Meshik, X.; Choi, M.; Farid, S.; Datta, D.; Lan, Y.; Poduri, S.; Sarkar, K.; Baterdene, U.; Huang, C. E.; Wang, Y.; Burke, P.; Dutta, M.; Stroscio, M. A Graphene and Aptamer Based Liquid Gated FET-Like Electrochemical Biosensor to Detect

https://dx.doi.org/10.1021/acsnano.0c04192
ACS Nano 2020, 14, 11637−11647

Adenosine Triphosphate. *IEEE Trans. Nanobioscience* **2015**, *14*, 967−972.

(38) Haustein, N.; Gutiérrez-Sanz, Ó.; Tarasov, A. Analytical Model to Describe the Effect of Polyethylene Glycol on Ionic Screening of Analyte Charges in Transistor-Based Immunosensing. *ACS Sensors* **2019**, *4*, 874−882.

(39) Tsormpatzoglou, A.; Papathanasiou, K.; Fasarakis, N.; Tassis, D. H.; Ghibaudo, G.; Dimitriadis, C. A. A Lambert-Function Charge-Based Methodology for Extracting Electrical Parameters of Nanoscale FinFETs. *IEEE Trans. Electron Devices* **2012**, *59*, 3299−3305.

(40) Fasarakis, N.; Tsormpatzoglou, A.; Tassis, D. H.; Pappas, I.; Papathanasiou, K.; Bucher, M.; Ghibaudo, G.; Dimitriadis, C. A. Compact Model of Drain Current in Short-Channel Triple-Gate FinFETs. *IEEE Trans. Electron Devices* **2012**, *59*, 1891−1898.

(41) Iacono, R.; Boyd, J. P. New Approximations to the Principal Real-Valued Branch of the Lambert W-Function. *Adv. Comput. Math.* **2017**, *43*, 1403−1436.

(42) Choi, Y.; Olsen, T. J.; Sims, P. C.; Moody, I. S.; Corso, B. L.; Dang, M. N.; Weiss, G. A.; Collins, P. G. Dissecting Single-Molecule Signal Transduction in Carbon Nanotube Circuits with Protein Engineering. *Nano Lett.* **2013**, *13*, 625−631.

(43) Rajan, N. K.; Routenberg, D. A.; Reed, M. A. Optimal Signal-to-Noise Ratio for Silicon Nanowire Biochemical Sensors. *Appl. Phys. Lett.* **2011**, *98*, 264107.

(44) Gao, X. P. A.; Zheng, G.; Lieber, C. M. Subthreshold Regime Has the Optimal Sensitivity for Nanowire FET Biosensors. *Nano Lett.* **2010**, *10*, 547−552.

(45) Bao, Z.; Sun, J.; Zhao, X.; Li, Z.; Cui, S.; Meng, Q.; Zhang, Y.; Wang, T.; Jiang, Y. Top-down Nanofabrication of Silicon Nanoribbon Field Effect Transistor (Si-NR FET) for Carcinoembryonic Antigen Detection. *Int. J. Nanomed.* **2017**, *12*, 4623−4631.

(46) Choi, Y.; Moody, I. S.; Sims, P. C.; Hunt, S. R.; Corso, B. L.; Perez, I.; Weiss, G. A.; Collins, P. G. Single-Molecule Lysozyme Dynamics Monitored by an Electronic Circuit. *Science (Washington, DC, U. S.)* **2012**, *335*, 319.

(47) Bouilly, D.; Hon, J.; Daly, N. S.; Trocchia, S.; Vernick, S.; Yu, J.; Warren, S.; Wu, Y.; Gonzalez, R. L.; Shepard, K. L.; Nuckolls, C. Single-Molecule Reaction Chemistry in Patterned Nanowells. *Nano Lett.* **2016**, *16*, 4679−4685.

(48) Perkins, F. K.; Friedman, A. L.; Cobas, E.; Campbell, P. M.; Jernigan, G. G.; Jonker, B. T. Chemical Vapor Sensing with Monolayer MoS_2. *Nano Lett.* **2013**, *13*, 668−673.

(49) Pugliese, K. M.; Gul, O. T.; Choi, Y.; Olsen, T. J.; Sims, P. C.; Collins, P. G.; Weiss, G. A. Processive Incorporation of Deoxynucleoside Triphosphate Analogs by Single-Molecule DNA Polymerase i (Klenow Fragment) Nanocircuits. *J. Am. Chem. Soc.* **2015**, *137*, 9587−9594.

https://dx.doi.org/10.1021/acsnano.0c04192
ACS Nano 2020, 14, 11637−11647